



LJMU Research Online

Song, W, He, Q, Rao, L, Zhang, S, Wang, J, Ren, X and Yang, Qi

**Heterogeneous nucleation interface between LaAlO₃ and niobium carbide:
First-principles calculation**

<http://researchonline.ljmu.ac.uk/id/eprint/17922/>

Article

Citation (please note it is advisable to refer to the publisher's version if you intend to cite from this work)

**Song, W, He, Q, Rao, L, Zhang, S, Wang, J, Ren, X and Yang, Qi (2022)
Heterogeneous nucleation interface between LaAlO₃ and niobium carbide:
First-principles calculation. Applied Surface Science, 606. p. 154731. ISSN
0169-4332**

LJMU has developed [LJMU Research Online](#) for users to access the research output of the University more effectively. Copyright © and Moral Rights for the papers on this site are retained by the individual authors and/or other copyright owners. Users may download and/or print one copy of any article(s) in LJMU Research Online to facilitate their private study or for non-commercial research. You may not engage in further distribution of the material or use it for any profit-making activities or any commercial gain.

The version presented here may differ from the published version or from the version of the record. Please see the repository URL above for details on accessing the published version and note that access may require a subscription.

For more information please contact researchonline@ljmu.ac.uk

<http://researchonline.ljmu.ac.uk/>

Heterogeneous nucleation interface between LaAlO₃ and niobium carbide: First-principles calculation

Wenwei Song ^a, Qizhen He ^a, Lixiang Rao ^a, Silong Zhang ^a, Jibo Wang ^{b,*}, Xuejun Ren ^c, Qingxiang Yang ^a,

^a State Key Lab of Metastable Materials Science & Technology, Yanshan University, Qinhuangdao 066004, PR China

^b College of Physics and Mechanical & Electrical Engineering, Longyan University, Longyan 364012, PR China

^c School of Engineering, Liverpool John Moores University, Liverpool L3 3AF, UK

Abstract

This paper aimed to investigate the interface relationship between LaAlO₃ and niobium carbide and possibility of LaAlO₃ as heterogeneous nucleus to refine niobium carbide by first principles method. Niobium carbide (NbC) is a transition metal carbide with high hardness. Primarily, the lattice mismatch relationship of LaAlO₃/NbC was calculated. Then, the interface models were established for the calculation of adhesive work and interface energy of LaAlO₃/NbC. Finally, the interfacial bonding types were analyzed with charge density, electron localized function (ELF) and partial density of states (PDOS). The results indicate that the interface mismatch between LaAlO₃(001) plane and NbC(111) plane is the smallest (8.4%), which indicates that LaAlO₃ can be as a moderately heterogeneous nucleus of NbC. Four interfacial models of LaAlO₃(110)/NbC(111) interface were established, which are named as LaAlO-NbT interface, LaAlO-CT interface, OT-NbT interface and OT-CT interface. The adhesive work of the OT-NbT interface is the largest (0.60 J/m²) and its interface energy is the smallest (4.02 J/m²), which indicates that the binding adhesive ability of the OT-NbT interface is the strongest. The bonding types of the OT-NbT interface are the combination of metallic, ionic and covalent bonds. Therefore, LaAlO₃ can act as the heterogeneous nucleus of NbC and refine it.

1. Introduction

With high hardness, high elastic modulus, high melting point, chemical inertness, Niobium carbide (NbC) has been applied in many engineering fields [1–2]. Numerous studies have been reported that NbC can be used as a special additive to reinforce the comprehensive mechanical properties of alloys by refining their microstructure [3–4]. Currently, many researches about the refinement effect of NbC have been reported. Li et al. [5] found that, for the preparation of WC-6Co functionally graded cemented carbide, NbC can refine carbide and improve its high-temperature hardness. Gao et al. [6] added NbC into CrMnFeCoNi high-entropy alloys, which lead to the refinement of microstructure and the enhancement of its tensile strength, yield strength and corrosion resistance. Wang et al. [7] demonstrated that, by adding NbC to Fe-0.2C-5Si-5Mn cold-rolled TRIP (Twinning Induced Plasticity) steel, NbC can delay austenite recrystallization, effectively refine austenite grains during hot rolling. Liu et al. [8] investigated the refinement mechanism of NbC on primary M₇C₃ carbides in hypereutectic Fe-Cr-C alloys, in which, NbC particle is the heterogeneous nucleus of primary M₇C₃ carbide and thereby refines it. Meanwhile, Tirumalasetty et al. [9] and Poddar et al. [10] found that the refinement effect of NbC is related with its size closely, and the smaller its size is, the better the refinement effect is. Therefore, it is significant to further refine the NbC size during the alloy solidification process. Because of its particular physical and chemical properties, rare earth (RE) elements are widely applied in industrial engineering, energy sources, electronics and other fields. Li et al. [11] studied that the microstructure can be effectively refined in Cu-Pb alloy by element Ce. It

was found that the lattice mismatch between CuPb₃ with Cu matrix at the grain boundary is small, and the tensile strength of the alloy is improved simultaneously. Zhang et al. [12] found that the TiBi₂ particle size can be significantly decreased by element Sc in Al-based composite coating. Xu et al. [13] studied that La₂O₃ led to the reduction of grain size in Al-P-Ti-TiC alloys, and the Brinell hardness is apparently improved to 39%. Zhou et al. [14] verified that when La₂O₃ was added in hypereutectic Fe-Cr-C coating, it can refine primary M₇C₃ carbide.

Wang et al. [15] found that La₂O₃ can react with element Al to form LaAlO₃, and LaAlO₃ can further refine the primary M₇C₃ carbides. Wang et al. [16] also found when La₂O₃ and TiC carbide were added into the hypereutectic Fe-Cr-C coating simultaneously, TiC could be refined by LaAlO₃. However, whether LaAlO₃ can act as the heterogeneous nucleus of NbC, and NbC can be refined by LaAlO₃ has not been reported before. Therefore, it is significant to theoretically explain the heterogeneous nucleation mechanism that LaAlO₃ refines NbC. Nowadays, first principles method has been applied to the interface relationship among crystalline materials. Lv et al. [17] reported the electronic structure and formation energies of the (Fe,M)₃C (M = Cr/ Mn/Co/Ni) interface. Xiao et al. [18] conducted theoretical studies on the stability of Cr₇C₃ carbide. However, the interface relationship between LaAlO₃ and NbC by the first principles calculation has not been reported at present. In the process of surfacing experiment, the hypereutectic Fe-Cr-C hardfacing alloy is made of flux-cored wire and open-arc surfacing by DC welding machine. In the preparation process of flux-cored wire, it is necessary to add a certain amount of Al powder as a deoxidizer, and La₂O₃ easily reacts with Al and its deoxidized product Al₂O₃ at high temperature to form LaAlO₃. Then, whether LaAlO₃ can serve as a heterogeneous nucleation substrate for NbC also needs further investigation. In this paper, LaAlO₃ was taken and the interface lattice mismatch relationship of LaAlO₃/NbC was calculated by Bramfitt's lattice mismatch degree theory. The LaAlO₃/NbC interface models were established by first principles method. Then, the interfacial adhesive work and interfacial energy between LaAlO₃ and NbC were calculated. The interfacial bonding type was investigated by charge density, electron local function (ELF) and partial density of states (PDOS) at the interface to illustrate the interface relationship of LaAlO₃/NbC and possibility of heterogeneous nucleation. It can provide theoretical basis for the analysis of LaAlO₃ acting as the heterogeneous nucleus of NbC.

2. Calculation and simulation methods

In this paper, Vienna Ab-initio Simulation Package (VASP) [19–21] based on density functional theory (DFT) was used to calculate the bulk and surface properties of the LaAlO₃ and NbC crystalline models and the bonding properties of LaAlO₃/NbC interface models. The generalized gradient approximation (General Gradient Approximation, GGA) exchange-correlation functional was used for the calculation [22]. The interaction between ion nuclei and valence electrons was described by a Planar Projector-Augmented Wave (PAW) [23]. The Monkhorst-Pack (M-P) method was used for the selection of the plane wave cutoff energy (ENCUT) and the Brillouin zone K-point mesh (Kmesh) [24]. The crystalline models for calculation are shown in Fig. 1. Among them, Fig. 1(a) is the crystalline structure of LaAlO₃, which belongs to the perovskite structure with space group PM-3M [25], and the lattice constant before sufficient relaxation is $a = b = c = 3.811 \text{ \AA}$. Fig. 1(b) is the crystalline structure of NbC, whose space group is sodium chloride structure of FM-3M [26], and the original lattice constant is $a = b = c = 4.400 \text{ \AA}$. The increase of the Brillouin zone K-point network and the ENCUT value can improve the calculation accuracy. Nevertheless, the calculation efficiency is also extended. The convergence test of the Brillouin zone K-point network and the plane wave truncation energy ENCUT value should be carried out before the relaxation of bulk models. The convergence criterion is that energy changes is less than $1 \times 10^{-5} \text{ eV/atom}$. The two K-point networks selected for the bulk structure optimization are $5 \times 5 \times 5$, and $5 \times 5 \times 1$ for surface convergence test and interface relationship calculation. The ENCUT value is 500 eV. The optimized result of LaAlO₃ is $a = b = c = 3.810 \text{ \AA}$, and the average error is 0.026%. The optimized result of NbC is 4.511 \AA , and the error is controlled within 2.5%. According to

Table 1, we compare the optimized results with the results in the Ref. [37–40], the results are extremely close and can be used for subsequent calculations. Calculation results are reliable and can be used for subsequent calculations.

3. Results and analysis

3.1. Structure properties

3.1.1. Structure properties of LaAlO₃

Electronic structures such as band structure and density of states (DOS) of crystalline models are usually calculated for solar cells and thermoelectric applications and so on [34–36]. The calculated results of band structure and DOS of LaAlO₃ are shown in Fig. 2. Fig. 2(a) is the band structure of LaAlO₃, in which, the dotted line is the position of Fermi level. It can be seen that the band structure of LaAlO₃ doesn't pass through the Fermi level. There is forbidden band width between its valence band and conduction band, and the band gap is 3.56 eV. Since the top of the valence band and the bottom of the conduction band of LaAlO₃ are facing each other, it is proved that LaAlO₃ has the characteristic of direct band gap semiconductor Fig. 2(b) is the total DOS map and the partial density of states (PDOS) of each atom. It can be seen that DOS of LaAlO₃ has no peak at the Fermi level, and the DOS at the Fermi level is close to 0, but not all zero, which indicates that the crystal primarily exhibits semiconductor properties. In the range of – 8eV to – 5eV, the DOS mainly comes from the contribution of Al and O atomic orbitals. Peak intensity of La atoms is very weak, which indicates that the outer electrons of the La atoms are transferred to the more electronegative O atoms. An ionic bond is formed between O atoms and La atoms. From – 7.5 eV to – 2.5 eV, there is a certain extent of orbital resonance and hybridization between the Al-3s, Al-3p orbitals and O-2p orbitals. It can be proved that there is a polar covalent bond between the Al atoms and O atoms. Therefore, the chemical bond in the bulk structure of LaAlO₃ is the mixture of ionic bond and covalent bond.

3.1.2. Structure properties of NbC

The band structure and DOS of NbC are shown in Fig. 3. Among them, Fig. 3(a) is the band structure of NbC, in which, the dashed line represents the position of Fermi level. The band structure of NbC passes through the Fermi level, which indicates that electrons can reach the conduction band from the valence band. It can be seen that NbC possesses metallic properties. Fig. 3(b) is a diagram of the total DOS and PDOS. It can be seen that the DOS of NbC has a peak at the Fermi level, and proves the existence of metallic bonds in the NbC crystalline structure from the contribution of Nb-4d orbitals. In the range of – 7.5 eV to – 1.5 eV, the peak shape of Nb4d and C-2p orbitals is consistent. It is shown that there are obvious interactions and orbital hybridization between Nb atoms and C atoms, which proves the formation of covalent bonds. Therefore, the chemical bonds in the crystalline structure of NbC is a combination of metallic bonds and covalent bonds.

3.2. Elastic modules and elastic anisotropy

3.2.1. Elastic modules

The calculated elastic matrix of LaAlO₃ is as follows:

$$C_{ij}(GPa) = \begin{pmatrix} 332 & 127 & 127 & & & \\ 127 & 332 & 127 & & & \\ 127 & 127 & 332 & & & \\ & & & 154 & & \\ & & & & 154 & \\ & & & & & 154 \end{pmatrix}$$

The calculated elastic matrix of NbC is as follows:

$$C_{ij}(GPa) = \begin{pmatrix} 706 & 105 & 105 & & & \\ 105 & 706 & 105 & & & \\ 105 & 105 & 706 & & & \\ & & & 179 & & \\ & & & & 179 & \\ & & & & & 179 \end{pmatrix}$$

The elastic constants [31–33] such as bulk modulus(K), Young’s modulus(E), shear modulus(G) and Poisson’s ratio(μ) as well as anisotropy of LaAlO₃ and NbC were investigated by ELATE software [27]. The calculation results of the elastic constants of LaAlO₃ and NbC are listed in Table 2. It can be seen that the that values of K, E, and G of NbC are all larger than those of LaAlO₃, which indicates that the compressive performance and deformation resistance of NbC are larger than those of LaAlO₃. The elastic modulus anisotropy for LaAlO₃ and NbC are listed in Table 3 and Table 4. It can be seen that the elastic modulus anisotropy values of LaAlO₃ is close to those of NbC. By comparing the elastic anisotropy of LaAlO₃ with those of NbC, the anisotropy of Young’s modulus and shear modulus of LaAlO₃ are smaller, which indicate that its microstructure is more uniform than that of NbC.

3.2.2. Elastic anisotropy

The 2D and 3D distributions of the elastic anisotropy for LaAlO₃ such as Young’s modulus, linear coefficient, shear modulus, and Poisson’s ratio are shown in Fig. 4. The elastic anisotropy of LaAlO₃ in Table 3 and the elastic anisotropy distribution diagram in Fig. 4 are combined in order to further analyze the elastic properties. Fig. 4(a) is the 2D and 3D distributions of Young’s modulus anisotropy of LaAlO₃. It can be seen that the anisotropy distribution of Young’s modulus in the three-dimension of x, y and z is comparative and large. The maximum value is 365.04GPa, the minimum index is 261.22GPa and the anisotropy value is 1.40. Fig. 4(b) is the 2D and 3D distributions of the linear coefficient anisotropy of LaAlO₃. It can be seen that the 3D distribution of the linear coefficient anisotropy is a perfect sphere with a value of 1.71 and no anisotropy exists. Fig. 4(c) and Fig. 4(d) are the 2D and 3D distributions of the shear modulus and Poisson’s ratio anisotropy of LaAlO₃, respectively. It can be seen that the distributions of the anisotropy values of shear modulus and Poisson’s ratio in the three dimension are exactly the same, while the distribution is more complicated. Among them, the maximum of shear modulus is 153.57GPa, the minimum value is 102.31GPa, and the anisotropy value is 1.50. The Poisson’s ratio can reach a maximum value of 0.35, a minimum value of 0.08, and an anisotropy value of 4.34. It can be seen that the Poisson’s ratio anisotropy value of LaAlO₃ is the largest among these four parameters. The 2D and 3D distribution diagrams of the anisotropy of Young’s modulus, linear coefficient, shear modulus and Poisson’s ratio of NbC are shown in Fig. 5. The results of elastic anisotropy of NbC were further analyzed in combination with Table 4 and Fig. 5. Fig. 5(a) is the 2D and 3D distributions of the Young’s modulus anisotropy for NbC. It is observed that the anisotropy of Young’s modulus in the three-dimensional of

x, y and z is relatively large and basically the same. The maximum value of Young's modulus is near to 678.96GPa, the minimum value is 449.11GPa, and the anisotropy can reach 1.51. Fig. 5(b) shows the 2D and 3D distributions of the linear coefficient anisotropy for NbC. It serves to show that the 3D distribution diagram of the linear coefficient anisotropy is a perfect sphere, so there is no anisotropy existing, and the linear coefficient value is nearly 1.09. Fig. 5(c) and Fig. 5(d) are 2D and 3D distributions of shear modulus and Poisson's ratio anisotropy of NbC. It can be seen that the anisotropy of shear modulus and Poisson's ratio are also basically similar in the three dimensional, but the distribution is more complex. The maximum value of the shear modulus is 300.26GPa, the minimum value is 179.00GPa, and the anisotropy value is 1.68. The Poisson's ratio has a maximum value of 0.37, a minimum value of 0.09, and an anisotropy of 3.96.

3.3. Lattice mismatch of LaAlO₃/NbC

According to the Bramfitt two-dimensional lattice mismatch theory [28], the Eq. (1) of the mismatch between LaAlO₃ and NbC is given by the following:

$$\delta_{(hkl)_s}^{(hkl)_n} = \sum_{i=1}^3 \frac{|d_{[uvw]_s}^i \cos\theta - d_{[uvw]_n}^i|}{d_{[uvw]_s}^i} / 3 \times 100\% \quad (1)$$

where (hkl)_s and (hkl)_n represents the low-index crystal plane of the substrate phase and nucleation phase, respectively; [uvw]_s and [uvw]_n represents a low-index crystal orientation on the (hkl)_s and (hkl)_n, respectively; d_{[uvw]_s and d_{[uvw]_n represents the atomic distance along the [uvw]_s and [uvw]_n, respectively; θ represent the angle between [uvw]_s and [uvw]_n.}}

It is pointed out that when the lattice mismatch between the substrate phase and nucleation phase is smaller than 6%, the substrate phase plays a very effective heterogeneous nucleation role for nucleation phase. When the lattice mismatch is 6–12%, the substrate phase plays a moderately heterogeneous nucleation role for nucleation phase. When the lattice mismatch is larger than 12%, the substrate phase cannot be regarded as the heterogeneous nuclei of nucleation phase.

The calculation results of the two-dimensional lattice mismatch between different crystalline planes of LaAlO₃/NbC are listed in Table 5. It is observed that the mismatch of LaAlO₃(110)/NbC(111) interface is the smallest, which is 8.4%. It indicates that LaAlO₃ can be moderately effective as the heterogeneous nucleus of NbC. Therefore, the LaAlO₃(110) plane and the NbC(111) plane are selected to establish the surface model and the interface model.

3.4. Surface convergence test

The surface models of the LaAlO₃ (110) plane and the NbC (111) plane were established, according to the calculated two-dimensional lattice mismatch. Here is a relevant principle that the upper and lower surface atoms of the surface models are the same. Based on the theory of surface convergence, vacuum layers with a thickness of 15 Å was added to cancel the interaction between the surface atoms. The surface models of LaAlO₃ (110) plane can be divided into LaAlO-Terminated and O-Terminated, and the surface models of NbC (111) plane is can be divided into two types: Nb-Terminated and C-Terminated, in which the surface model of NbC plane is non-polar surface. The surface models established based on Bramfitt theory are shown in Fig. 6. To simplify the calculation, the values can be approaching as follows:

$$\mu_{La}^{slab} \approx \mu_{La}^{bulk}, \mu_{Al}^{slab} \approx \mu_{Al}^{bulk}, \mu_{O}^{slab} \approx \mu_{O}^{bulk}, \mu_{Nb}^{slab} \approx \mu_{Nb}^{bulk}, \mu_{C}^{slab} \approx \mu_{C}^{bulk} \quad (2)$$

3.4.1. Surface convergence test of LaAlO₃ (110)

Since the surface models are sufficiently relaxed, the atoms have been redistributed and energy of the bulk system is further reduced. It tends to a more stable state. The chemical potential equation of the surface models of LaAlO₃ is as follows:

$$\mu_{LaAlO_3}^{slab} = \mu_{LaAlO_3}^{bulk} = \mu_{La}^{slab} + \mu_{Al}^{slab} + \mu_O^{slab} \quad (3)$$

where $\mu_{LaAlO_3}^{bulk}$ is the system energy after bulk optimization of LaAlO₃; μ_{La}^{slab} , μ_{Al}^{slab} , μ_O^{slab} are the chemical potential of La, Al, O atoms. Among them, the calculated chemical potential of O atom is -4.905 eV.

The equation for calculating the surface energy of LaAlO₃ is as follows:

$$\sigma_{LaAlO_3(110)} = \frac{1}{2A} (E_{slab} - N_{La}\mu_{La}^{slab} - N_{Al}\mu_{Al}^{slab} - N_O\mu_O^{slab}) \quad (4)$$

where $\sigma_{LaAlO_3(110)}$ is the surface energy after bulk optimization of LaAlO₃; E_{slab} is the surface energy of the surface models with a certain number of atomic layers; A is the surface area of the surface models; N_{La} , N_{Al} , N_O are numbers of La, Al, O.

In the LaAlO-Terminated surface model of LaAlO₃ (110), the number of atoms satisfies the following relationship:

$$N_{La} = N_{Al}N_O = 3N_{Al} - 2 \quad (5)$$

Combining Eqs. (3), (4) and (5), the surface energy formula of the LaAlO-Terminated surface model is obtained as follows:

$$\sigma_{LaAlO_3(110)} = \frac{1}{2A} [E_{slab} - N_{Al}\mu_{LaAlO_3}^{bulk} + 2\mu_O^{slab}] \quad (6)$$

In the surface model of LaAlO₃ (110) O-Terminated, the number of atoms satisfies the following relationship:

$$N_{La} = N_{Al}N_O = 3N_{Al} + 2 \quad (7)$$

Combining Eqs. (3), (4) and (7), the surface energy equation of the O-Terminated surface model is obtained as follows:

$$\sigma_{LaAlO_3(110)} = \frac{1}{2A} [E_{slab} - N_{Al}\mu_{LaAlO_3}^{bulk} - 2\mu_O^{slab}] \quad (8)$$

Surface energies of LaAlO-Terminated and O-Terminated models with different numbers of termination layers on the LaAlO₃ (110) plane were calculated according to Eqs. (6) and (8). The results are listed in Table 6. When the number of atomic layers is the 9th layer, the LaAlO₃ (110) surface energy of LaAlO-Terminated converges to 6.14 J/m², and the energy change is really slight. When the number of atomic layers reaches the 7th layer, the LaAlO₃ (110) surface energy of O-Terminated surface model converges to 2.12 J/m².

3.4.2. Surface convergence test of NbC (111)

The equation for calculating the chemical potential of the surface model of NbC is as follows:

$$\mu_{NbC}^{slab} = \mu_{NbC}^{bulk} = \mu_{Nb}^{slab} + \mu_C^{slab} \quad (9)$$

where μ_{NbC}^{bulk} is the system energy after bulk optimization of NbC; μ_{Nb}^{slab} , μ_C^{slab} are the chemical potential of Nb and C atoms. Among them, the calculated chemical potential of C atom is - 9.093 eV.

The equation for calculating the surface energy of NbC is as follows:

$$\sigma_{NbC(111)} = \frac{1}{2A} (E_{slab} - N_{Nb}\mu_{Nb}^{slab} - N_C\mu_C^{slab}) \quad (10)$$

where $\mu_{NbC(111)}$ is the surface energy of NbC (111) surface model; N_{Nb} , N_C are numbers of Nb atoms and C atoms in the NbC surface models.

Combining Eqs. (9) and (10), the final surface energy calculation formula of the NbC (111) surface is obtained as follows:

$$\sigma_{NbC(111)} = \frac{1}{2A} [E_{slab} - N_{Nb}\mu_{NbC}^{bulk} + (N_{Nb} - N_C)\mu_C^{slab}] \quad (11)$$

The surface energies of Nb-Terminated and C-Terminated models for NbC(111) surface obtained by Eqs. (11) are listed in Table 7. It is observed that the surface energy of Nb-Terminated model for the NbC (111) surface converges in the seventh layer, and the surface energy is 2.50 J/m². The surface energy of the C-Terminated can be well converged to 3.23 J/m² in the seventh layer.

Based on the above calculation results of surface energy convergence test, the 9th-layer LaAlO₃ (110) of LaAlO-Terminated model, the 7th-layer LaAlO₃ (110) of O-Terminated model, the 7th-layer NbC (111) of Nb-Terminated model, and the 7th-layer NbC (111) of C-Terminated model are selected to establish successive interface models.

3.5. Interfacial bonding properties

3.5.1. Interfacial structure and stability

According to the calculation results of two-dimensional lattice mismatch and the surface energy convergence test, four interface models were finally established below. The interface models of the top view and its bottom (001) plane are shown in Fig. 7. Fig. 7(a,a') is the interface model and top view of LaAlO-NbT; Fig. 7(b,b') is the interface model and top view of LaAlO-CT; Fig. 7(c,c') is the interface model and top view of OT-NbT; Fig. 7(d,d') is the interface model and top view of OT-CT. In order to ensure that the above-mentioned four interfaces are more stable, the energy under different interface distances was calculated and the interface distance with the lowest energy was selected for the subsequent calculation of interface binding work and interface energy to ensure the rationality and accuracy of the results. The relationship between the interface distance and energy of the four interface models is shown in Fig. 8.

The four interface models with the lowest energy and the corresponding interface distances screened out in Fig. 8 are as follows. The interface distance corresponding to LaAlO-NbT is 2.8 Å. The interface distance corresponding to LaAlO-CT is 2.2 Å. The interfacial distance corresponding to OT-NbT is 1.8 Å, and the corresponding interface spacing of OT-CT is 1.2 Å.

3.5.2. Interface adhesive work

The adhesive work (W_{ad}) indicates the strength of the interface binding ability. The equation for calculating the W_{ad} of the LaAlO₃(110)/NbC(111) interface models is as follows:

$$W_{ad} = \frac{1}{A}(E_{LaAlO_3} + E_{NbC} - E_{LaAlO_3/NbC}) \quad (12)$$

where W_{ad} is adhesive work of the LaAlO₃(110)/NbC(111) interface models; E_{LaAlO_3} is the surface energy of the LaAlO₃ (110) surface models; E_{NbC} is the surface energy of the NbC (111) surface model; $E_{LaAlO_3/NbC}$ is the energy of the LaAlO₃(110)/NbC(111) interface models calculated by DFT.

The W_{ad} was calculated for the interface model of the above interface distance, and the results are listed in Table 8. It is observed that the W_{ad} of the four interfaces is as follows:

$$W_{ad_{OT-CT}} > W_{ad_{OT-NbT}} > W_{ad_{LaAlO-CT}} = W_{ad_{LaAlO-NbT}};$$

and the W_{ad} of OT-Nb and OT-CT interface models is the largest which both are 0.60 J/m²

3.5.3. Interface energy

The interface energy (γ) represents the resistance to interface formation. The equation for calculating the γ of the LaAlO₃(110)/NbC (111) interface model is as follows: 3.5.3. Interface energy The interface energy (γ) represents the resistance to interface formation. The equation for calculating the γ of the LaAlO₃(110)/NbC (111) interface model is as follows:

$$\gamma = \sigma_{LaAlO_3} + \sigma_{NbC} - W_{ad} \quad (13)$$

where γ is interface energy of the LaAlO₃(110)/NbC(111) interface models; σ_{LaAlO_3} is the surface energy of the LaAlO₃ (110) surface model; σ_{NbC} is the surface energy of the NbC (111) surface models.

The γ of the LaAlO₃(110)/NbC(111) interface models were calculated according to Eqs. (13), as listed in Table 9. It can be seen that the γ of the four interfaces is as follows:

$$\gamma_{LaAlO-CT} > \gamma_{LaAlO-NbT} > \gamma_{OT-CT} > \gamma_{OT-NbT}.$$

The γ of the OT-NbT interface model is the smallest, which is 4.02 J/ m² . Considering the factors of adhesive work and interface energy, it is concluded that the interface structure of OT-NbT is the easiest to form.

3.6. Interfacial electronic structure

The electronic structures of the above four interface models were calculated and analyzed in order to further analyze the bonding properties of the interface. The charge transfer situation at the interface represents the bonding situation between interfacial atoms. It was characterized by calculating the charge density of the interface [29], local density function (ELF) [30], and partial density of states (PDOS).

3.6.1. Interfacial charge density

The schematic diagrams of the internal and its bottom (001) plane of the two LaAlO interface models are shown in Fig. 9. The position of the dotted line in the Figs. 9-11 is the position of the interface. Among them, Fig. 9(a) and (b) are the charge density diagrams of the interior of the LaAlO-NbT interface model and the cross-section of the (001) surface layer. There is obvious diffusion of O atoms inside the interface, and the charge density around Al atoms in the surface layer is small, which

indicates that more electrons are lost. Fig. 9(c) and (d) are the charge density maps of the interior and (001) surface section of the LaAlO-CT interface model. It is apparent that C atoms in the interface and (001) plane are diffused. The interaction between O atoms and C atoms, Al atoms is very strong, and the surrounding charges have partial charge overlap phenomenon, which proves the formation of chemical bonds. The atoms on both sides of the interfaces are far apart after fully relaxing, which make it difficult to form bonds. Therefore, the interfacial bonding properties is relatively poor.

The schematic diagrams of the internal and its bottom (001) plane of two OT interface models are shown in Fig. 10. Fig. 10(a) and (b) are the charge density diagrams of the interior of the OT-NbT interface model and the (001) section. At the interface of the fully relaxed structural model, it can be observed intuitively that there is obvious diffusion of O atoms at the interface, both inside and on the surface, and there is an obvious charge overlap with Nb atoms, which indicates the formation of strong chemical bonds. Fig. 10(c) and (d) are the charge density maps of the interior and surface of the OT-CT interface model. The strong diffusion of C atoms and O atoms can be seen in both the interior and the surface of the interface, and there is a partial overlap at the interface. There is an evident interaction between C atoms and O atoms, which indicated the formation of strong chemical bonds.

3.6.2. Interfacial electron local function

The electronic structure of the interface was analyzed by calculating the electron local function (ELF) of the interface models, and the bonding properties of the interface are further studied by combining the PDOS at the interface. The calculation equation of ELF is as follows:

$$ELF = 1/[1 + (\frac{D(r)}{Dh_r})^2] \quad (14)$$

where $D(r)$ is the real gas density; Dh_r is the uniform electron gas density. The ELF value is between 0 and 1, $ELF = 1$ represents complete electron localization in the region, $ELF = 1/2$ indicates a uniform electron gas state, and $ELF = 0$ refers to complete electron delocalization in the region. The diagrams of the (001) plane for four interface structures, and the dotted line in the figure is the position at the interface are shown in Fig. 11. Fig. 11(a) is the ELF image of the LaAlO-NbT interface. It can be seen that the bonding type between atoms at the interface is mainly covalent bonds. Fig. 11(b) is the ELF diagram of the LaAlO-CT interface. It is observed that the ELF values between C and O atoms at the interface are between 0.6 and 0.9, and the ELF values between Al atoms and O and C atoms are between 0.2 and 0.3, which indicated that the main bonding types at the interface are mainly the combination of covalent and ionic bonds. Fig. 11(c) is the ELF image of the OT-NbT interface. It is obvious that the ELF value between Nb atom and O atom ranges from 0.1 to 0.4, and the ELF value between C atom and O atom ranges from 0.5 to 0.8, which indicated that the bonding type at the interface is mainly ionic bond with covalent bonds. Fig. 11(d) is the diagram of the OT-CT interface. It can be seen that the ELF values between C atoms and O atoms are between 0.4 and 0.8, and the ELF values of O atoms and Nb atoms range from 0.2 to 0.5, which indicate that the main bonding types at the interface are covalent and ionic bonds.

3.6.3. Partial density of the states (PDOS)

After fully relaxed of the four interface models, the interface charges are redistributed locally. In order to further study the bonding types and properties of the four interface models, the partial density of the states (PDOS) was calculated, as shown in Fig. 12. The position of the dashed line in the figure is Fermi level. The DOS of the first layer atoms and the inner atoms on both sides of the interface were analyzed, and the bonding properties at the interface were further studied. Fig. 12(a) is the PDOS map of the LaAlO-NbT interface. From -18 eV to -15 eV, the waveforms of O atoms and Nb atoms are

basically the same, while the center of gravity is different. Between -12 eV and -2 eV, the orbital waveforms of O atoms and C atoms are basically the same, which can be seen that the LaAlO-NbT interface has common types of valence and metal bonds. Fig. 12(b) is the PDOS diagram of the LaAlO-CT interface. Between -18 eV and -15 eV, the peak shape of O atom and C atom is similar. From -7 eV to -2 eV, the waveforms of La, Al, C, Nb atoms are close, and it can be seen that there are ionic bonds and covalent bonds. Fig. 12(c) is the PDOS image of the OT-NbT interface. In the range from -15 eV to -10 eV, the peaks of O atoms and C atoms are basically the same, and the peaks are close to each other, which proves the formation of covalent bonds. Fig. 12(d) is the PDOS image of the OT-CT interface. From -13 eV to -11 eV, the peak shapes and peaks of C atoms and O atoms are similar. Between -11 eV \sim -9 eV, the peak shape of O atoms and C atoms and O atoms are consistent, while the center of gravity is different, and the change is small, which indicates that there are covalent bonds, ionic bonds and metal bonds at the interface.

Based on Bramfitt's lattice mismatch degree theory, the minimum mismatch of LaAlO₃/NbC is 8.4%, which is 6–12%. It indicates that LaAlO₃ as the substrate phase, plays a moderately heterogeneous nucleation role for nucleation phase NbC. Therefore, NbC can be refined by LaAlO₃. For four interface types of LaAlO₃(110)/NbC(111) such as LaAlONbT interface, LaAlO-CT interface, OT-NbT interface, and OT-CT interface, the adhesive work is as follows: $W_{adOT-CT} > W_{adOT-NbT} > W_{adLaAlO-CT} = W_{adLaAlO-NbT}$, and the interface energy is as follows: $\gamma_{LaAlO-NbT} > \gamma_{LaAlO-CT} > \gamma_{OT-CT} > \gamma_{OT-NbT}$. It indicates that the interface energy of OT-NbT is the smallest, which is 0.60 J/m², and its adhesive work is the largest, which is 4.02 J/m². Therefore, it reveals that LaAlO₃ and NbC are easily combined on OT-NbT interface.

4. Conclusion

- According to the calculation results of the bulk properties of LaAlO₃ and NbC, the bond types of LaAlO₃ are the combination of ionic bond and covalent bond. NbC is the mixture of metallic bond and covalent bond. The bulk modulus of LaAlO₃ is 195GPa, the Young's modulus is 320GPa, the shear modulus is 131GPa, and the Poisson's ratio is 0.23. The bulk modulus of NbC is 305GPa, the Young's modulus is 533GPa, and the shear modulus is 221GPa, Poisson's ratio is 0.21.
- Based on Bramfitt's two-dimensional lattice mismatch theory, the minimum mismatch of LaAlO₃/NbC is 8.4%, which indicates that LaAlO₃ can be as a moderately heterogeneous nucleus of NbC carbide.
- Four interface models of LaAlO₃(110)/NbC(111) were established, named as LaAlO-NbT interface, LaAlO-CT interface, OT-NbT interface, and OT-CT interface. The adhesive work of OT-NbT interface is the largest, which is 0.60 J/m². The interface energy of OT-NbT is the smallest, which is 4.02 J/m². Therefore, it indicates that LaAlO₃ and NbC are easily combined on OT-NbT interface.
- The bonding types of the OT-NbT interface are the combination of metallic, ionic and covalent bonds.

CRedit authorship contribution statement

Wenwei Song: Conceptualization, Methodology, Software, Data curation, Investigation, Writing – original draft. Qizhen He: Formal analysis. Lixiang Rao: Methodology. Silong Zhang: Visualization. Jibo Wang: Funding acquisition, Validation. Xuejun Ren: Funding acquisition, Conceptualization, Supervision. Qingxiang Yang: Funding acquisition, Project administration, Writing – review & editing.

Declaration of Competing Interest

The authors declare that they have no known competing financial interests or personal relationships that could have appeared to influence the work reported in this paper.

Data availability

Data will be made available on request.

Acknowledgement

The authors would like to express their gratitude for projects supported by the National Natural Science Foundation of China (No. 51771167), European Union's Horizon 2020 Research and innovation program through a Marie Skłodowska-Curie Research and Innovation Staff Exchange Funding (Grant Agreement No.823786)., Hebei Province Innovation Ability Promotion Project (22567609H) and Natural Science Foundation of Fujian Province(No.2020J05196).

References

- [1] B. Vishwanadh, A. Arya, R. Tewari, G.K. Dey, Formation mechanism of stable NbC carbide phase in Nb-1Zr-0.1C (wt.%) alloy, *Acta Mater.* 144 (2018) 470–483, <https://doi.org/10.1016/j.actamat.2017.11.007>.
- [2] E. Coy, L. Yate, D.P. Valencia, W. Aperador, K. Siuzdak, P. Torruella, E. Azanza, S. Estrade, I. Iatsunskiy, F. Peiro, X. Zhang, J. Tejada, R.F. Ziolo, High Electrocatalytic Response of a Mechanically Enhanced NbC Nanocomposite Electrode Toward Hydrogen Evolution Reaction, *ACS Appl. Mater. Interfaces* 9 (2017) 30872–30879, <https://doi.org/10.1021/acsami.7b10317>.
- [3] M. Woydt, S. Huang, J. Vleugels, H. Mohrbacher, E. Cannizza, Potentials of niobium carbide (NbC) as cutting tools and for wear protection, *Int. J. Refract Metal Hard Mater.* 72 (2018) 380–387, <https://doi.org/10.1016/j.ijrmhm.2018.01.009>.
- [4] T. Lin, Q. Li, Y. Han, K. Song, X. Wang, H. Shao, J. Dong, H. Wang, X. Deng, Effects of Nb and NbC additives on microstructure and properties of WC-Co-Ni cemented carbides, *Int. J. Refract Metal Hard Mater.* 103 (2022), 105782, <https://doi.org/10.1016/j.ijrmhm.2022.105782>.
- [5] X. Li, Y. Liu, W. Wei, M. Du, K. Li, J. Zhou, K. Fu, Influence of NbC and VC on microstructures and mechanical properties of WC-Co functionally graded cemented carbides, *Mater. Des.* 90 (2016) 562–567, <https://doi.org/10.1016/j.matdes.2015.10.156>.
- [6] N. Gao, D.H. Lu, Y.Y. Zhao, X.W. Liu, G.H. Liu, Y. Wu, G. Liu, Z.T. Fan, Z.P. Lu, E. P. George, Strengthening of a CrMnFeCoNi high-entropy alloy by carbide precipitation, *J. Alloy. Compd.* 792 (2019) 1028–1035, <https://doi.org/10.1016/j.jallcom.2019.04.121>.
- [7] X.D. Wang, B.X. Huang, L. Wang, Y.H. Rong, Microstructure and Mechanical Properties of Microalloyed High-Strength Transformation-Induced Plasticity Steels, *Metall. Mater. Trans. A* 39 (2008) 1–7, <https://doi.org/10.1007/s11661-007-9366-4>.
- [8] S. Liu, Z. Wang, Z. Shi, Y. Zhou, Q. Yang, Experiments and calculations on refining mechanism of NbC on primary M7C3 carbide in hypereutectic Fe-Cr-C alloy, *J. Alloy. Compd.* 713 (2017) 108–118, <https://doi.org/10.1016/j.jallcom.2017.04.167>.
- [9] G.K. Tirumalasetty, M.A. van Huis, C.M. Fang, Q. Xu, F.D. Tichelaar, D.N. Hanlon, J. Sietsma, H.W. Zandbergen, Characterization of NbC and (Nb, Ti)N nanoprecipitates in TRIP assisted multiphase steels, *Acta Mater.* 59 (2011) 7406–7415, <https://doi.org/10.1016/j.actamat.2011.08.012>.
- [10] D. Poddar, P. Cizek, H. Beladi, P.D. Hodgson, The evolution of microbands and their interaction with NbC precipitates during hot deformation of a Fe–30Ni–Nb model austenitic steel, *Acta Mater.* 99 (2015) 347–362, <https://doi.org/10.1016/j.actamat.2015.08.003>.
- [11] H. Li, X. Liu, Y. Li, S. Zhang, Y. Chen, S. Wang, J. Liu, J. Wu, Effects of rare earth Ce addition on microstructure and mechanical properties of impure copper containing Pb, *Trans. Nonferrous Metals Soc. China* 30 (2020) 1574–1581, [https://doi.org/10.1016/S1003-6326\(20\)65320-1](https://doi.org/10.1016/S1003-6326(20)65320-1).
- [12] T. Zhang, K. Feng, Z. Li, H. Kokawa, Effects of rare earth elements on the microstructure and wear properties of TiB₂ reinforced aluminum matrix composite coatings: Experiments and first principles calculations, *Appl. Surf. Sci.* 530 (2020), 147051, <https://doi.org/10.1016/j.apsusc.2020.147051>.

- [13] C.L. Xu, H.Y. Wang, Y.F. Yang, H.-Y. Wang, Q.C. Jiang, Effect of La₂O₃ in the Al–P–Ti–TiC–La₂O₃ modifier on primary silicon in hypereutectic Al–Si alloys, *J. Alloy. Compd.* 421 (2006) 128–132, <https://doi.org/10.1016/j.jallcom.2005.11.034>.
- [14] Y. Zhou, Y. Yang, X. Qi, Y. Jiang, J. Yang, X. Ren, Q. Yang, Influence of La₂O₃ addition on microstructure and wear resistance of Fe–Cr–C cladding formed by arc surface welding, *J. Rare Earths* 30 (2012) 1069–1074, [https://doi.org/10.1016/S1002-0721\(12\)60180-X](https://doi.org/10.1016/S1002-0721(12)60180-X).
- [15] J. Wang, X. Xing, Y. Zhou, S. Liu, X. Qi, Q. Yang, Formation mechanism of ultrafine M₇C₃ carbide in a hypereutectic Fe–25Cr–4C–0.5Ti–0.5Nb–0.2N–2LaAlO₃ hardfacing alloy layer, *J. Mater. Res. Technol.* 9 (2020) 7711–7720, <https://doi.org/10.1016/j.jmrt.2020.05.039>.
- [16] J. Wang, J. Yang, C. Wang, Y. Zhou, X. Xing, Y. Yang, Q. Yang, First-principles calculation on LaAlO₃ as the heterogeneous nucleus of TiC, *Comput. Mater. Sci.* 101 (2015) 108–114, <https://doi.org/10.1016/j.commatsci.2015.01.024>.
- [17] Z.Q. Lv, F.C. Zhang, S.H. Sun, Z.H. Wang, P. Jiang, W.H. Zhang, W.T. Fu, Firstprinciples study on the mechanical, electronic and magnetic properties of Fe₃C, *Comput. Mater. Sci.* 44 (2008) 690–694, <https://doi.org/10.1016/j.commatsci.2008.05.006>.
- [18] B. Xiao, J.D. Xing, J. Feng, C.T. Zhou, Y.F. Li, W. Su, X.J. Xie, Y.H. Cheng, A comparative study of Cr₇C₃, Fe₃C and Fe₂B in cast iron both from ab initio calculations and experiments, *J. Phys. D: Appl. Phys.* 42 (11) (2009) 115415.
- [19] G. Kresse, J. Hafner, Ab initio molecular dynamics for liquid metals, *Phys. Rev. B.* 47 (1993) 558–561, <https://doi.org/10.1103/PhysRevB.47.558>.
- [20] G. Kresse, J. Hafner, Ab initio molecular-dynamics simulation of the liquidmetal–amorphous–semiconductor transition in germanium, *Phys. Rev. B.* 49 (1994) 14251–14269, <https://doi.org/10.1103/PhysRevB.49.14251>.
- [21] G. Kresse, J. Furthmüller, Efficient iterative schemes for ab initio total-energy calculations using a plane-wave basis set, *Phys. Rev. B.* 54 (1996) 11169–11186, <https://doi.org/10.1103/PhysRevB.54.11169>.
- [22] J.P. Perdew, K. Burke, M. Ernzerhof, Generalized Gradient Approximation Made Simple, *Phys. Rev. Lett.* 77 (1996) 3865–3868, <https://doi.org/10.1103/PhysRevLett.77.3865>.
- [23] P.E. Blochl, Projector augmented-wave method, *Phys. Rev. B* 50 (1994) 17953–17979, <https://doi.org/10.1103/PhysRevB.50.17953>.
- [24] H.J. Monkhorst, J.D. Pack, Special points for Brillouin-zone integrations, *Phys. Rev. B* 13 (1976) 5188–5192, <https://doi.org/10.1103/PhysRevB.13.5188>.
- [25] A. Boudali, B. Amrani, M. Driss khodja, A. Abada, K. Amara, First-principles study of structural, elastic, electronic, and thermal properties of LaAlO₃ perovskite, *Comput. Mater. Sci.* 45 (4) (2009) 1068–1072.
- [26] J.H. Jang, C.H. Lee, Y.U. Heo, D.W. Suh, Stability of (Ti, M)C (M=Nb, V, Mo and W) carbide in steels using first-principles calculations, *Acta Mater.* 60 (2012) 208–217, <https://doi.org/10.1016/j.actamat.2011.09.051>.
- [27] R. Gaillac, P. Pullumbi, F.-X. Coudert, ELATE: an open-source online application for analysis and visualization of elastic tensors, *J. Phys.: Condens. Matter.* 28 (2016), 275201, <https://doi.org/10.1088/0953-8984/28/27/275201>.
- [28] B.L. Bramfitt, The effect of carbide and nitride additions on the heterogeneous nucleation behavior of liquid iron, *METALLURGICAL TRANSACTIONS.* (n.d.) 9.
- [29] M. Wolloch, G. Levita, P. Restuccia, M.C. Righi, Interfacial Charge Density and Its Connection to Adhesion and Frictional Forces, *Phys. Rev. Lett.* 121 (2018), 026804, <https://doi.org/10.1103/PhysRevLett.121.026804>.
- [30] K. Koumpouras, J.A. Larsson, Distinguishing between chemical bonding and physical binding using electron localization function (ELF), *J. Phys.: Condens. Matter.* 32 (31) (2020) 315502.
- [31] Z. Wu, E. Zhao, H. Xiang, X. Hao, X. Liu, J. Meng, Crystal structures and elastic properties of superhard IrN₂ and IrN₃ from first principles, *Phys. Rev. B* 76 (2007), 054115, <https://doi.org/10.1103/PhysRevB.76.054115>.

- [32] D. Fan, S. Lu, A.A. Golov, A.A. Kabanov, X. Hu, D-carbon: Ab initio study of a novel carbon allotrope, *J. Chem. Phys.* 149 (11) (2018) 114702.
- [33] F. Mouhat, F.X. Coudert, Necessary and sufficient elastic stability conditions in various crystal systems, *Phys. Rev. B* 90 (2014), 224104, [https://doi.org/ 10.1103/PhysRevB.90.224104](https://doi.org/10.1103/PhysRevB.90.224104).
- [34] M.A. Ali, S.A. Dar, A.A. AlObaid, T.I. Al-Muhimeed, H.H. Hegazy, G. Nazir, G. Murtaza, Appealing perspectives of structural, electronic, mechanical, and thermoelectric properties of $\text{Ti}_2(\text{Se, Te})\text{Cl}_6$ vacancy-ordered double perovskites, *J. Phys. Chem. Solids* 159 (2021), 110258, [https://doi.org/10.1016/j. jpcs.2021.110258](https://doi.org/10.1016/j.jpcs.2021.110258).
- [35] H. Albalawi, B.U. Haq, G. Nazir, T. Ghrib, N.A. Kattan, Q. Mahmood, A.I. Aljameel, M. Morsi, S. Bouzgarrou, Study of new double perovskite halides $\text{Rb}_2\text{Ti}(\text{Cl}/\text{Br})_6$ for solar cells and thermoelectric applications, *Mater. Today Commun.* 32 (2022) 104106.
- [36] M.A. Amin, G. Nazir, Q. Mahmood, J. Alzahrani, N.A. Kattan, A. Mera, H. Mirza, A. Mezni, M.S. Refat, A.A. Gobouri, T. Altalhi, Study of double perovskites X_2InSbO_6 ($\text{X} = \frac{1}{4} \text{Sr, Ba}$) for renewable energy; alternative of organic- inorganic perovskites, *Journal of materials research and technology*. (n.d.) 10.
- [37] X. Luo, B. Wang, Y. Zheng, First-principles study on energetics of intrinsic point defects in LaAlO_3 , *Phys. Rev. B* 80 (2009), 104115, [https://doi.org/10.1103/ PhysRevB.80.104115](https://doi.org/10.1103/PhysRevB.80.104115).
- [38] C.J. Howard, B.J. Kennedy, B.C. Chakoumakos, Neutron powder diffraction study of rhombohedral rare-earth aluminates and the rhombohedral to cubic phase transition, *J. Phys.: Condens. Matter*. 12 (2000) 349–365, [https://doi.org/ 10.1088/0953-8984/12/4/301](https://doi.org/10.1088/0953-8984/12/4/301).
- [39] E.I. Isaev, S.I. Simak, I.A. Abrikosov, R. Ahuja, Y.K. Vekilov, M.I. Katsnelson, A. I. Lichtenstein, B. Johansson, Phonon related properties of transition metals, their carbides, and nitrides: A first-principles study, *J. Appl. Phys.* 101 (12) (2007) 123519.
- [40] A. Teresiak, H. Kubsch, X-ray investigations of high energy ball milled transition metal carbides, *Nanostruct. Mater.* 6 (1995) 671–674, [https://doi.org/10.1016/ 0965-9773\(95\)00147-6](https://doi.org/10.1016/0965-9773(95)00147-6).

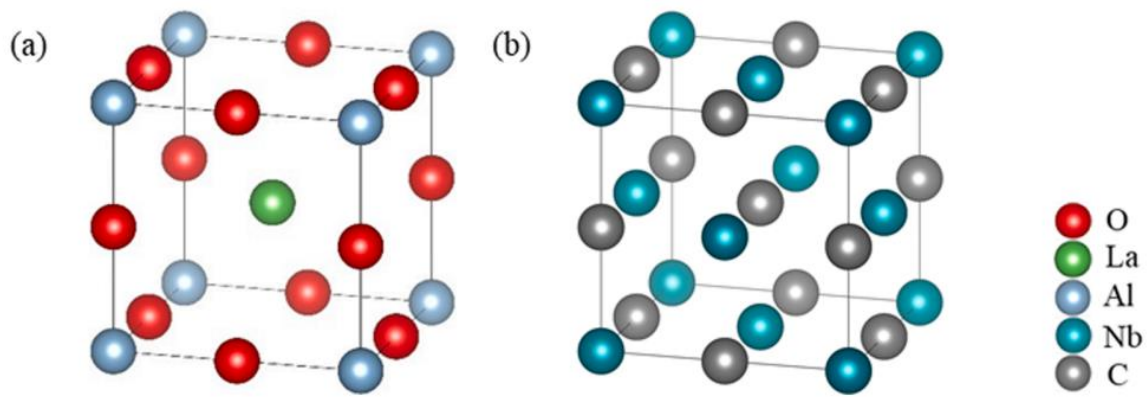


Fig. 1. Crystalline models. (a) LaAlO₃; (b) NbC.

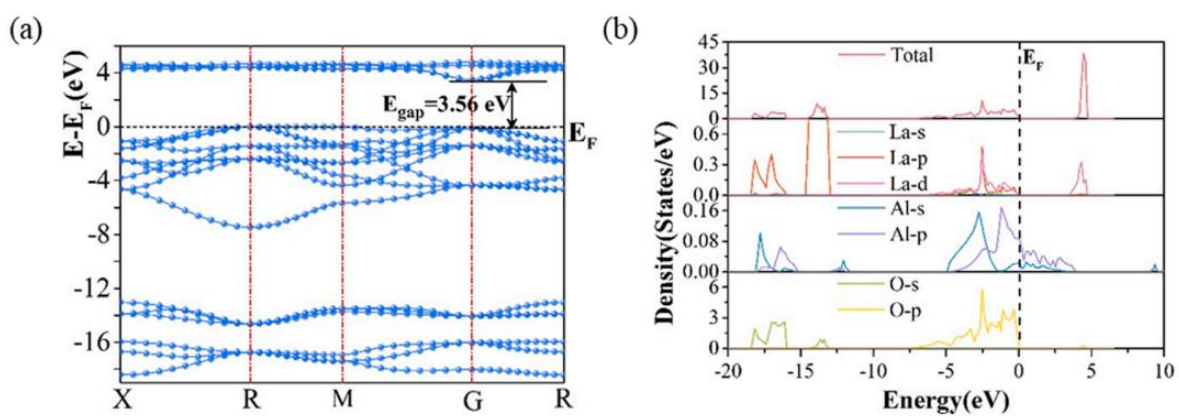


Fig. 2. Band structure and DOS of LaAlO₃. (a) Band structure; (b) DOS.

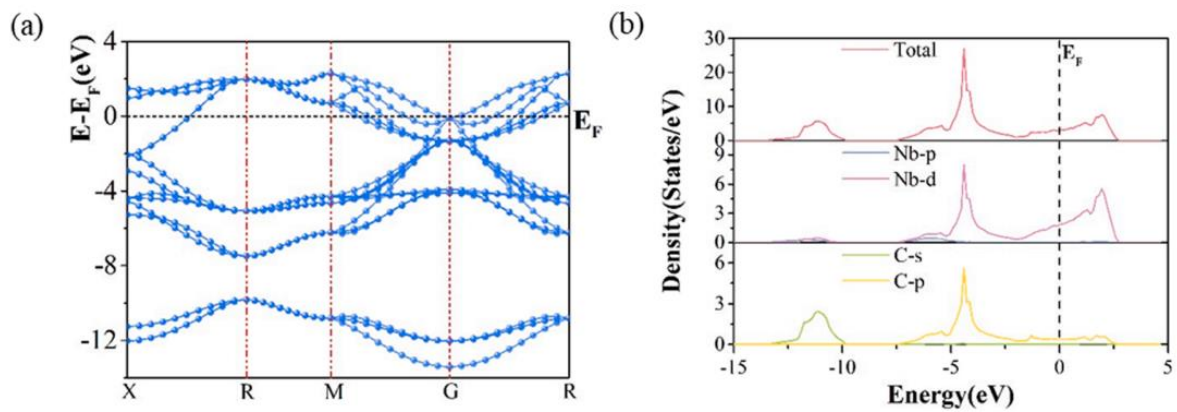


Fig. 3. Band structure and DOS of NbC. (a) Band structure; (b) DOS.

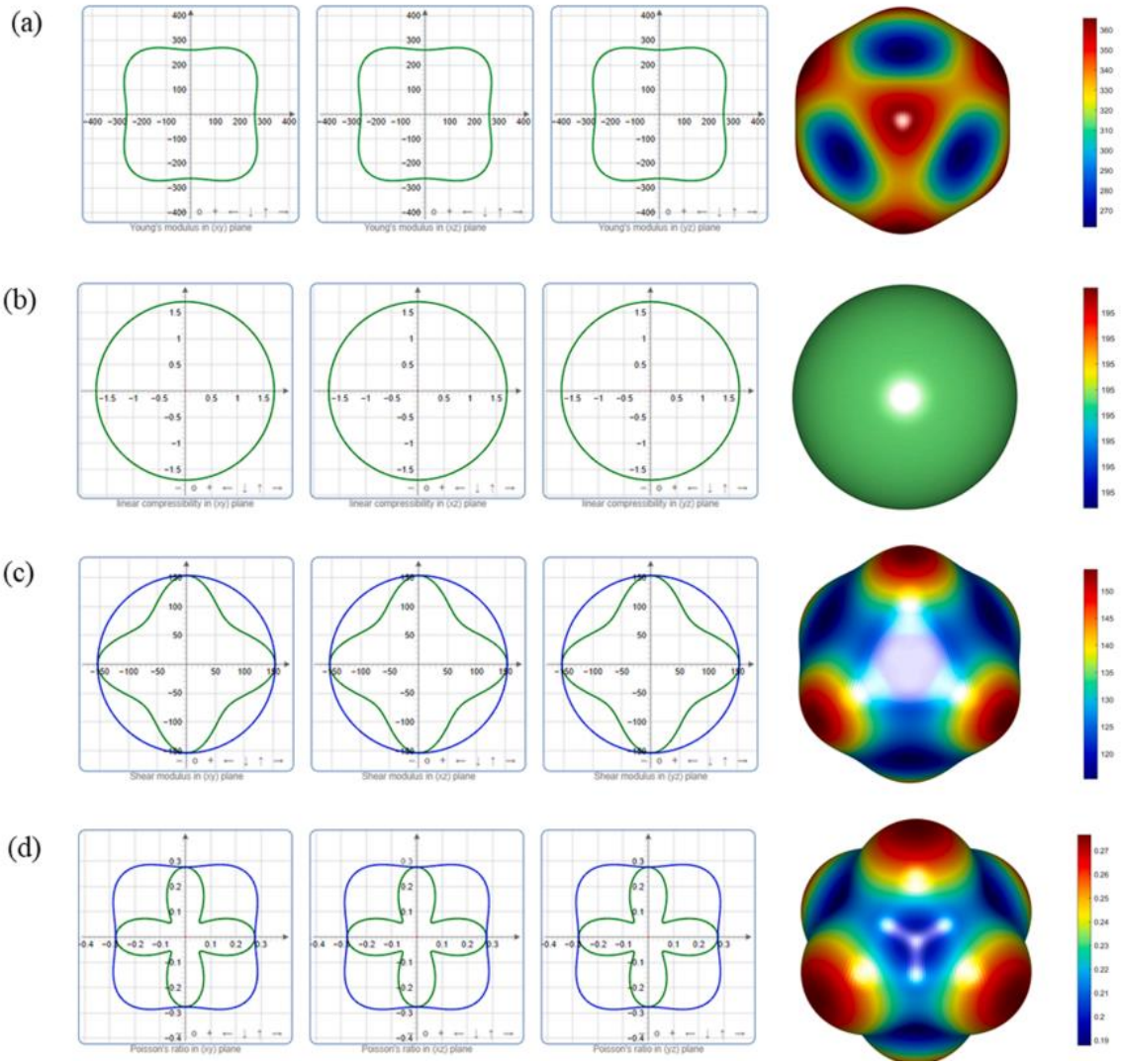


Fig. 4. 2D and 3D distributions of elastic constant anisotropy for LaAlO₃. (a) Young's modulus; (b) Linear coefficient; (c) Shear modulus; (d) Poisson's ratio.

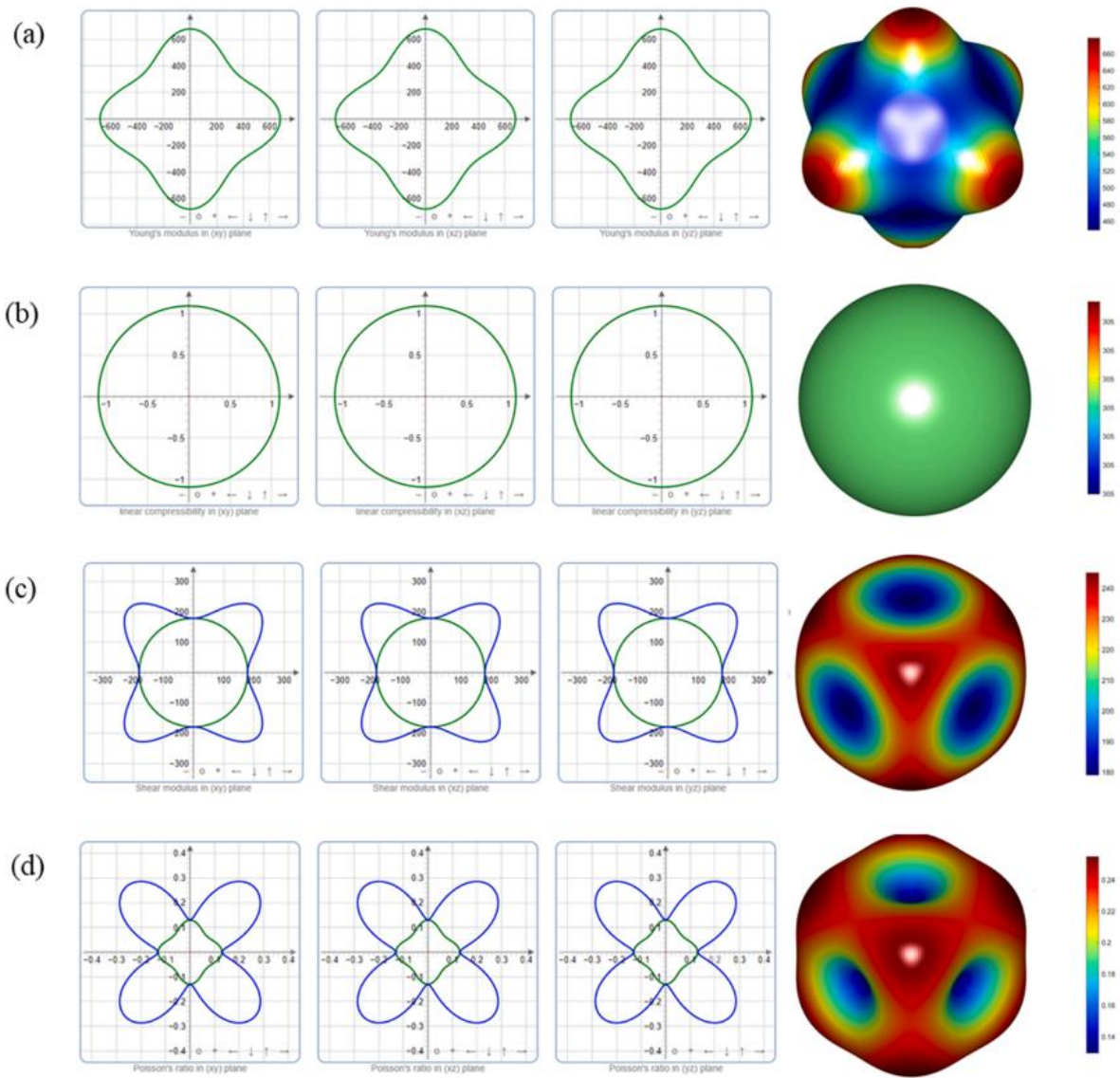


Fig. 5. 2D and 3D distributions of elastic constant anisotropy for NbC. (a) Young's modulus; (b) Linear coefficient; (c) Shear modulus; (d) Poisson's ratio.

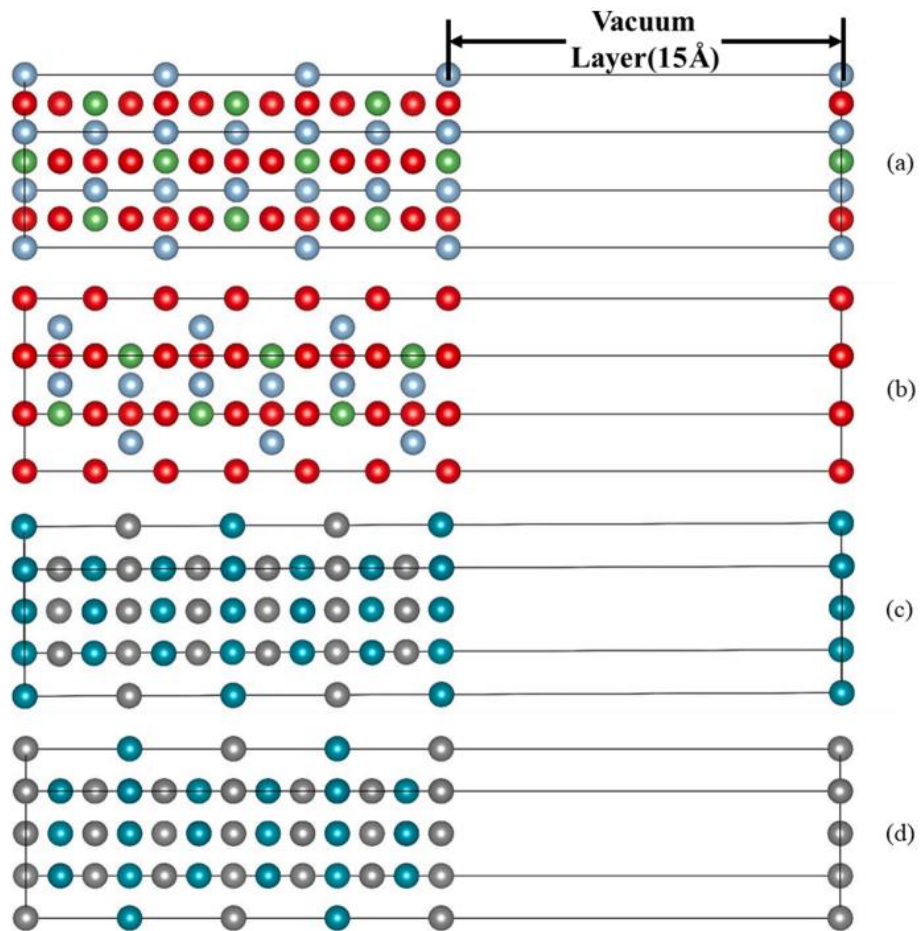


Fig. 6. Diagrams of surface models for LaAlO₃ and NbC. (a) LaAlO₃ (110) surface model of LaAlO-Terminated; (b) LaAlO₃ (110) surface model of O-Terminated; (c) NbC (111) surface model of Nb-Terminated; (d) NbC (111) surface model of C-Terminated.



Fig. 7. Four interface structures and their top views. (a) LaAlO-NbT interface; (b) LaAlO-CT interface; (c) OT-NbT interface; (d) OT-CT interface.

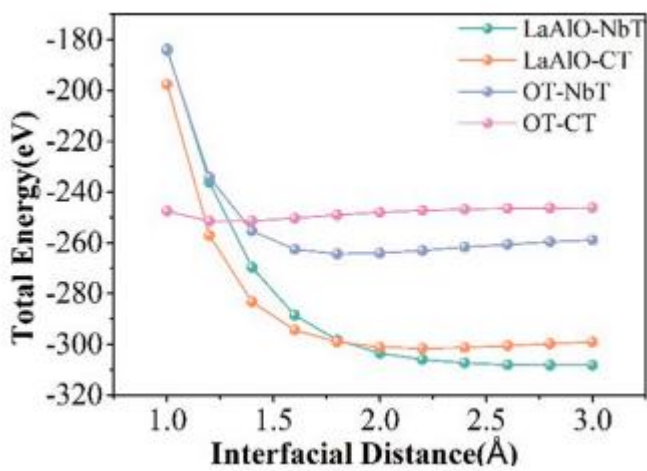


Fig. 8. Relationship diagram of the interfacial distance energy of the four interface models.

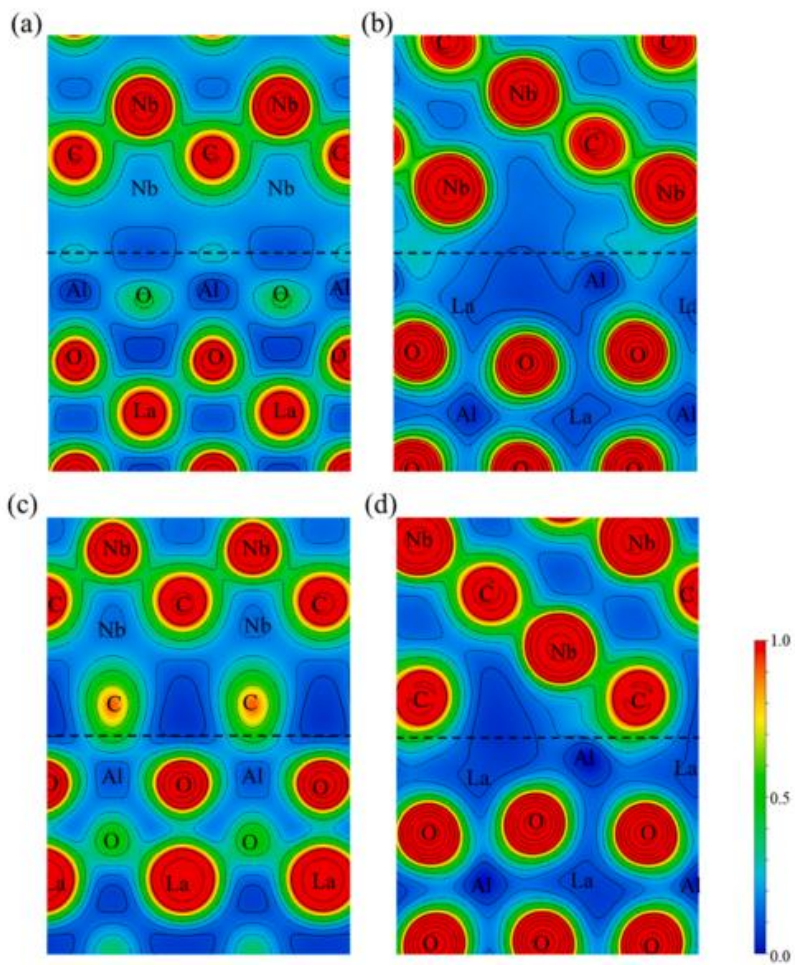


Fig. 9. Charge density maps of the interior and (001) plane of the two LaAlO interfacial structures. (a) Inside LaAlO-NbT interface; (b) (001) surface charge density map; (c) Inside LaAlO-CT interface; (d) (001) surface charge density map.

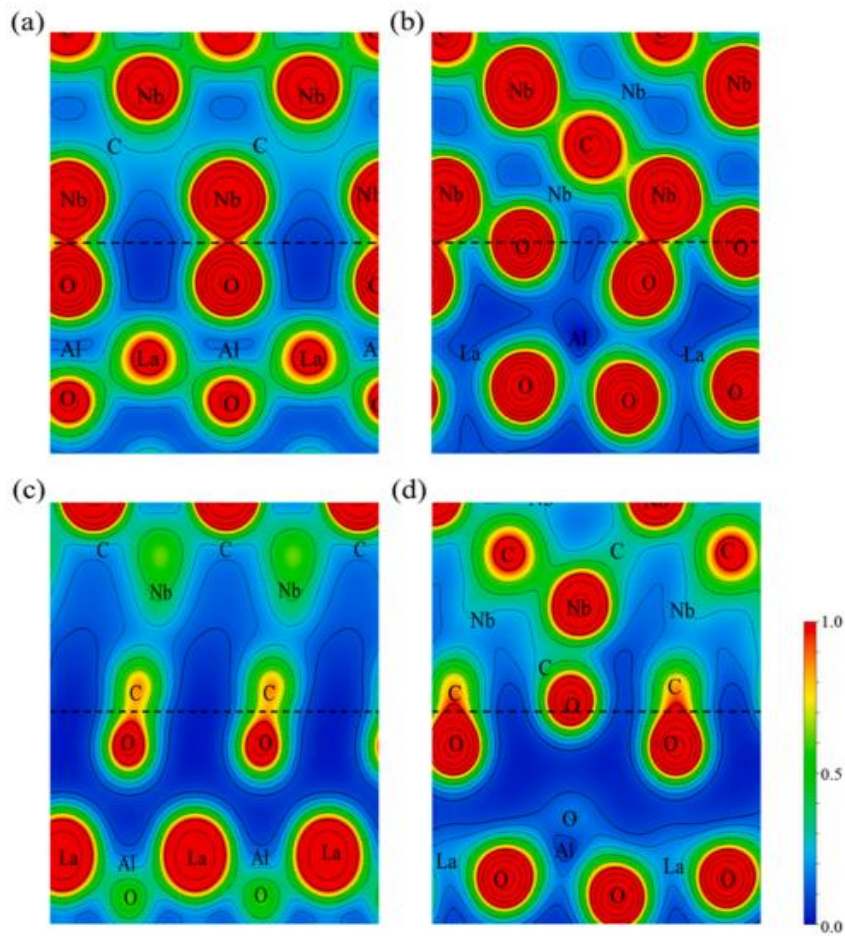


Fig. 10. Charge density maps of the interior and (001) plane of the two OT interfacial structures. (a) Inside OT-NbT interface; (b) (001) surface charge density map; (c) Inside OT-CT interface; (d) (001) surface charge density map.

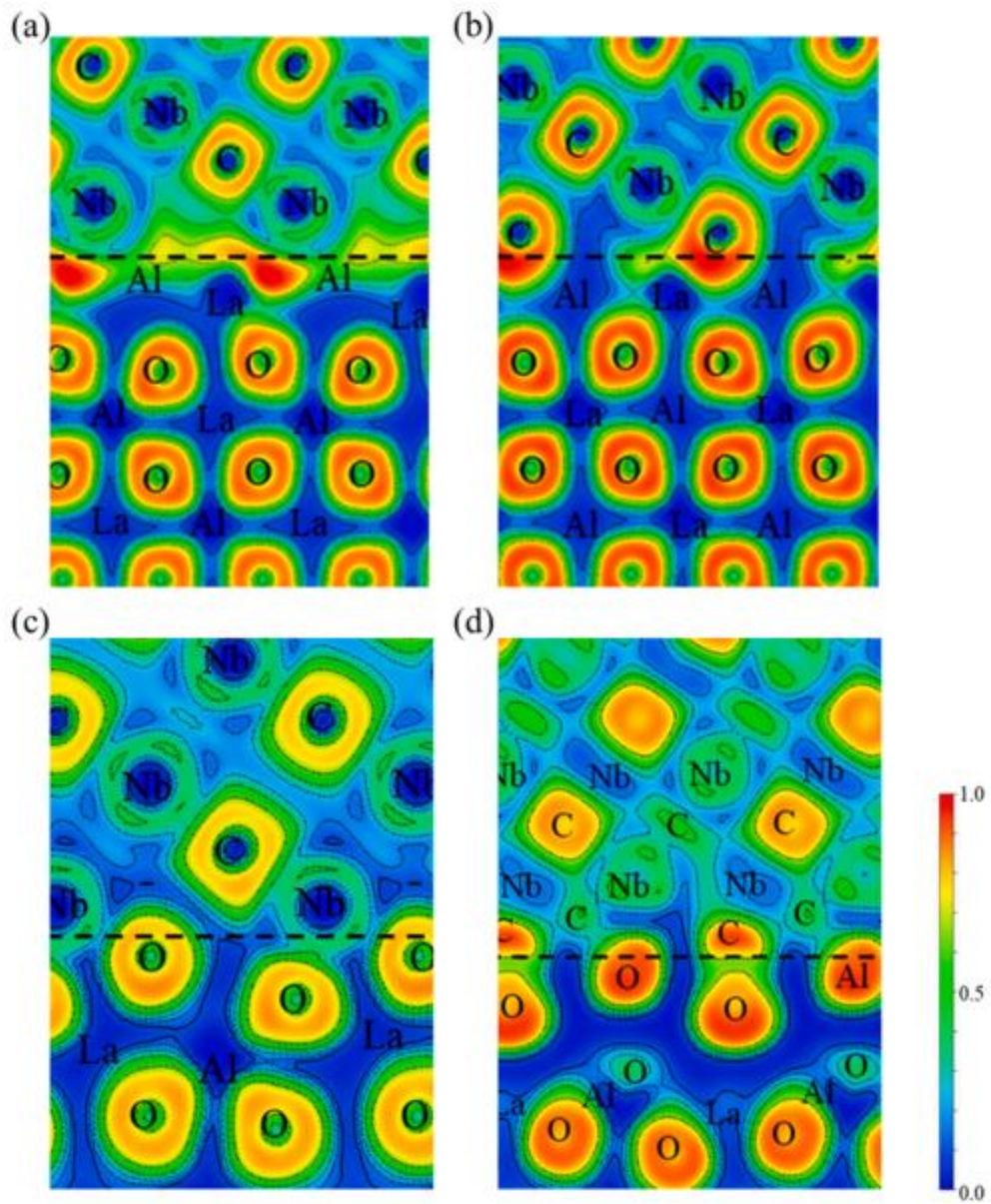


Fig. 11. ELF diagram of the (001) plane of the LaAlO₃ (110)/NbC(111) interfacial models. (a) LaAlO-NbT interface; (b) LaAlO-CT interface; (c) OT-NbT interface; (d) OT-CT interface.

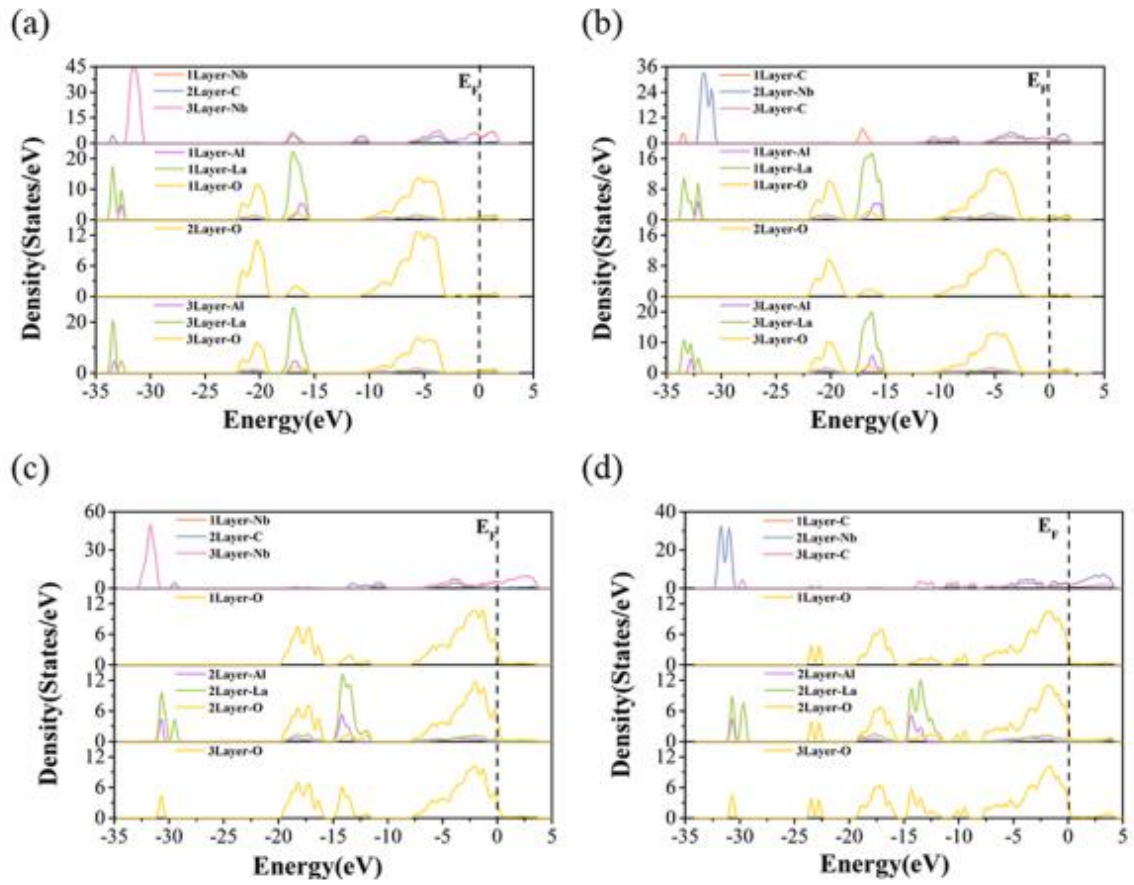


Fig. 12. PDOS diagram of the LaAlO₃ (110)/NbC(111) interfacial models. (a) LaAlO-NbT interface; (b) LaAlO-CT interface; (c) OT-NbT interface; (d) OTCT interface.

Table 1

Calculated lattice constants of the bulk LaAlO₃ and NbC compared with other references and experimental data.

Structures	Method	a = b = c(Å)	Volume(Å ³)
LaAlO ₃	GGA-PBE _{this work}	3.810	55.306
	GGA-PBE ^a	3.807	55.176
	Exp. ^b	3.829	56.138
NbC	GGA-PBE _{this work}	4.400	85.184
	GGA-PBE ^c	4.476	89.675
	Exp. ^d	4.471	89.374

^a Ref. [37].

^b Ref. [38].

^c Ref. [39].

^d Ref. [40].

Table 2

Calculated elastic modulus of LaAlO₃ and NbC.

	Bulk modulus (K)	Young's modulus(E)	Shear modulus (G)	Poisson's ratio (μ)
LaAlO ₃	195GPa	320GPa	131GPa	0.23
NbC	305GPa	533GPa	221GPa	0.21

Table 3

Calculated elastic anisotropy of LaAlO₃.

LaAlO ₃	Bulk modulus(GPa)		Linear coefficient (TPa ⁻¹)		Shear modulus(GPa)		Poisson's ratio	
	E _{min}	E _{max}	β _{min}	β _{max}	G _{min}	G _{max}	μ _{min}	μ _{max}
Values	261.22	365.01	1.71	1.71	102.31	153.57	0.08	0.35
Anisotropy	1.40		1.00		1.50		4.34	

Table 4

Calculated elastic anisotropy of NbC.

NbC	Bulk modulus(GPa)		Linear coefficient (TPa ⁻¹)		Shear modulus(GPa)		Poisson's ratio	
	E _{min}	E _{max}	β _{min}	β _{max}	G _{min}	G _{max}	μ _{min}	μ _{max}
Values	449.11	678.96	1.09	1.09	179.00	300.26	0.09	0.37
Anisotropy	1.51		1.00		1.68		3.96	

Table 5

Calculated two-dimensional lattice mismatch of LaAlO₃/NbC low exponential plane.

Matching face	LaAlO ₃ (110)//NbC(111)			LaAlO ₃ (110)//NbC(110)			LaAlO ₃ (001)//NbC (100)		
	[001]	[1 $\bar{1}$ 0]	[1 $\bar{1}$ 1]	[200]	[020]	[110]	[200]	[020]	[110]
[uvw]La ₂ O ₃	[1 $\bar{1}$ 0]	[11 $\bar{1}$]	[10 $\bar{1}$]	[002]	[1 $\bar{1}$ 0]	[11 $\bar{2}$]	[01 $\bar{1}$]	[011]	[010]
[uvw]NbC	[1 $\bar{1}$ 0]	[11 $\bar{1}$]	[10 $\bar{1}$]	[002]	[1 $\bar{1}$ 0]	[11 $\bar{2}$]	[01 $\bar{1}$]	[011]	[010]
θ(°)	0	0	2.421	0	0	0	0	0	0
d La ₂ O ₃ (Å)	3.811	5.389	6.6	7.621	5.389	9.334	7.621	7.621	5.389
dNbC(Å)	3.186	5.519	6.373	9.013	6.373	11.038	6.373	6.373	4.506
δ(%)	8.4			15.4			18.5		

Table 6

Surface energy of LaAlO₃ (110) Surface Models for LaAlO-Terminated and O-Terminated.

Layer(N)	3	5	7	9	11	13
$\sigma_{\text{LaAlO-Terminated}}(\text{J/m}^2)$	6.01	6.16	6.13	6.14	6.14	6.14
$\sigma_{\text{O-Terminated}}(\text{J/m}^2)$	2.01	2.12	2.12	2.13	2.14	2.14

Table 7

Surface energy of NbC (111) Surface Models for Nb-Terminated and C-Terminated.

Layer(N)	3	5	7	9	11	13
$\sigma_{\text{Nb-Terminated}}(\text{J/m}^2)$	3.18	2.74	2.50	2.51	2.55	2.54
$\sigma_{\text{C-Terminated}}(\text{J/m}^2)$	3.63	3.33	3.23	3.23	3.22	3.22

Table 8

Adhesive work of LaAlO₃ (110)/NbC (111) Interface Model.

Interface	LaAlO-NbT	LaAlO-CT	OT-NbT	OT-CT
Wad (J/m ²)	-0.18	0.22	0.60	0.60

Table 9

Interface energy of LaAlO₃ (110)/NbC (111) Interface Model.

Interface	LaAlO-NbT	LaAlO-CT	OT-NbT	OT-CT
γ (J/m ²)	8.82	9.15	4.02	4.75